PHYSICAL REVIEW MATERIALS **7**, 043601 (2023)

Hybrid interatomic potential for Sn

Mashroor S. Nitol,[1,*] Khanh Dang,[1] Saryu J. Fensin,[1,†] Michael I. Baskes,[1,2]
Doyl E. Dickel,[3,‡] and Christopher D. Barrett[3]
[1] *Los Alamos National Laboratory, Los Alamos, New Mexico 87545, USA*
[2] *Department of Materials Science & Engineering, University of North Texas, Denton, Texas 76203, USA*
[3] *Department of Mechanical Engineering, Mississippi State University, Starkville, Mississippi 39762, USA*

(Received 8 November 2022; revised 31 January 2023; accepted 17 March 2023; published 3 April 2023)

To design materials for extreme applications, it is important to understand and predict phase transitions and their influence on material properties under high pressures and temperatures. Atomistic modeling can be a useful tool to assess these behaviors. However, this can be difficult due to the lack of fidelity of the interatomic potentials in reproducing this high pressure and temperature extreme behavior. Here, a hybrid EAM-R—which is the combination of embedded atom method (EAM) and rapid artificial neural network potential—for Tin (Sn) is described which is capable of accurately modeling the complex sequence of phase transitions between different metallic polymorphs as a function of pressure. This hybrid approach ensures that a basic empirical potential like EAM is used as a lower energy bound. By using the final activation function, the neural network contribution to energy must be positive, assuring stability over the whole configuration space. This implementation has the capacity to reproduce density functional theory results at 6 orders of magnitude slower than a pair potential for molecular dynamics simulation, including elastic and plastic characteristics and relative energies of each phase. Using calculations of the Gibbs free energy, it is demonstrated that the potential precisely predicts the experimentally observed phase changes at temperatures and pressures across the whole phase diagram. At 10.2 GPa, the present potential predicts a first-order phase transition between body-centered tetragonal (BCT) β-Sn and another polymorph of BCT-Sn. This structure transforms into body-centered cubic near the experimentally reported value at 33 GPa. Thus, the Sn potential developed in this paper can be used to study complex deformation mechanisms under extreme conditions of high pressure and strain rates unlike existing potentials. Moreover, the framework developed in this paper can be extended for different material systems with complex phase diagrams.

DOI: 10.1103/PhysRevMaterials.7.043601

I. INTRODUCTION

There is significant interest in the structural, electrical, and thermodynamic properties of Sn [1–4] due to the prevalence of Sn-containing materials such as Sn-Pb and Sn-Li alloys in a wide variety of contemporary technological applications [5–8]. To understand the deformation mechanisms in tin and its alloys in detail, atomic-scale simulations are an efficient way to complement experimental data that provide macroscopic insights into the overall mechanical behavior [9,10]. While atomistic simulations can provide atomic-scale information, their accuracy depends on the precision of interatomic potentials. Hence, it is of the utmost significance that dependable interatomic potentials be readily available. In this paper, we develop an interatomic potential form to represent the complex structures of Sn especially under high pressures and temperatures.

In the periodic table, Sn marks the transition zone between the semiconducting group-14 elements Si and Ge and the heavier metallic member Pb. Like Sn, when subjected to high pressure, both silicon and germanium are known to go through a complicated sequence of phase transitions that can result in a wide variety of metallic polymorphs [11–13]. The diamond-structured (α-Sn, $Fd\bar{3}m$) phase of Sn can be found at temperatures < 286 K. Above this temperature, Sn crystallizes into a form known as body-centered tetragonal (BCT, β-Sn, $I4_1/amd$), which is characterized by metallic bonding [3,14]. An early high-pressure investigation revealed that the polymorph that was generated at pressures > 10 GPa had a tetragonally deformed structure BCT ($I4/mmm$) with an axial ratio of $c/a < 0.91$ [15]. Above P ~44 GPa, the axial ratio increases, and the body-centered cubic (BCC) structure was identified using the x-ray diffraction pattern [16]. These observations were made in conjunction with the fact that, under increasing pressure, the axial ratio increased from the BCT to the BCC phase. Several investigations have found different coexisting phases at high pressures between 40 and 55 GPa as BCT [16] and 50–152 GPa as BCC. Fairly recent theoretical [17] and experimental [18] studies showed that the BCC polymorph remained stable up to 157 GPa, and above that pressure, it transformed into an hexagonal close-packed (HCP)-Sn ($P6_3/mmc$) structure. The unit cells of experimentally observed phases up to 157 GPa are depicted in Fig. 1. The presence of these allotropic phases makes the system complex, and it is a challenge to represent these phases

---

[*] mash@lanl.gov
[†] saryuj@lanl.gov
[‡] doyl@me.msstate.edu

2475-9953/2023/7(4)/043601(18)

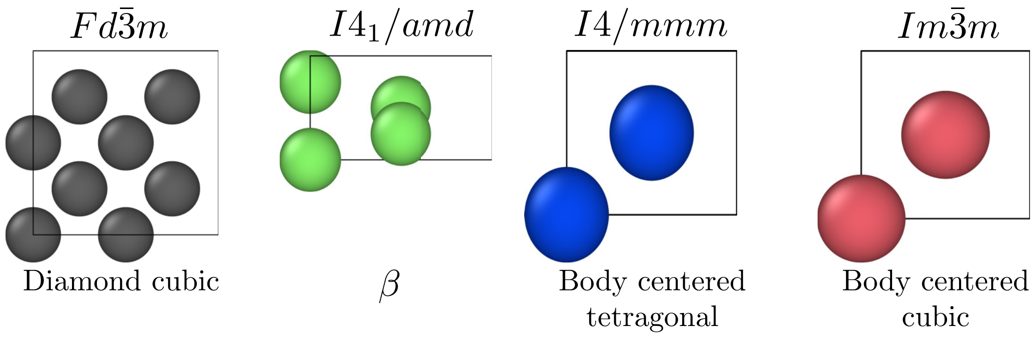

FIG. 1. Unit cells of the crystal structures and space groups of the four different solid phases of Sn examined in this paper. The coloring of the various phases will remain the same throughout the text.

accurately using interatomic potentials. Although the embedded atom method (EAM) model [19] predicts the BCT and BCC phases at high pressure, it fails to predict the β-Sn phase as a stable phase under ambient conditions [20]. In contrast, the many-body interatomic potentials [21–23] derived using the modified EAM (MEAM) [24] were better at representing the β-Sn and liquid phases. An alternative interatomic potential has been developed by Ko *et al.* [25] (MEAM-Ko) based on the second nearest-neighbor (NN) MEAM [26]. In comparison with previously reported MEAM potentials, the MEAM-Ko potential significantly improves the reliability of numerous physical metrics, especially β-Sn phase properties at ambient pressure, but fails to predict high-pressure phases (>5 GPa) under dynamic conditions. In general, the empirical potentials developed previously cannot simultaneously predict stable Sn phases at ambient and high-pressure phases. Due to the differences in the underlying physical and chemical models relevant to Sn, traditional functional forms of potentials are varied and, to a considerable degree, inconsistent. Due to the constraint imposed by the functional form, modeling multiphase systems with both covalent and metallic bonding presents a substantial challenge.

To overcome some of these challenges, a direction has emerged in this area in which interatomic potentials are being generated using machine learning (ML) techniques [27–31]. ML potentials have exploded into an exciting research field in computational materials science that has received widespread attention. In materials research, the introduction and development of ML skills may be viewed as part of a bigger journey toward data-driven methodologies which can accelerate the discovery of materials. In simpler terms, the fundamental concept underlying ML is to minimize the importance of physical or chemical intuition to determine the functional form of interatomic potentials in favor of mathematical interpolation using known reference data provided by quantum-mechanical computations [32–37]. This strategy represents a significant departure from conventional methods, with the objective of reaching a comparable result by capturing the fundamental physical science of interatomic bonding. To a high degree, and for many different configurations and architectures, ML approaches can reproduce first-principles data. Many different material systems, such as alloys and oxides, have benefited from their application [38–44].

One such ML potential is the rapid artificial neural network (RANN), which is generated using the methodology of the MEAM formalism, which includes exponential decay of interaction strength with distance, angular dependent interactions, and the use of known modulus and NN distance to determine metaparameters and construct features [45,46]. This potential style permits network topologies of any size and activation function, and the structural fingerprint computation uses single looping summations over the neighbor list of a target atom, improving processing speed. In addition, angular screening has been included to enhance efficiency by restricting the number of neighbors included and to increase predictive power by combining fingerprint filtering and smoothing when atoms cross the radial cutoff [47,48]. RANN has shown promise in modeling multiphase systems, e.g., Ti and Zr, giving it an advantage for modeling even more complex systems like Sn. In this paper, we demonstrate how we combine EAM with the RANN potential (EAM-R) to reproduce the structural and mechanical properties of four experimentally observed phases in Sn under pressure.

II. METHODOLOGY

A. Density functional theory training database

Modeling the many atomic environments accurately requires a large database covering a wide variety of structures. The energies and forces of different structures are calculated using QUANTUM ESPRESSO (QE) [49], version 6.4.1, with the generalized gradient approximation (GGA) exchange-correlation functional and Perdew-Burke-Ernzerhof (PBE) [50] pseudopotential. Rehn *et al.* [51] suggests that the AM05 [52] exchange-correlation functionals, rather than PBE [50], are in better agreement with experimental findings. It is found here that the equilibrium volume using PBE is $\sim$1 Å^3/atom (5%) smaller than that obtained using AM05. It is not unusual for the density functional theory (DFT) cohesive energy, equilibrium volume, and bulk modulus to vary with the pseudopotential and disagree with experimental data. Since AM05 is not included in the free DFT package QE, the PBE exchange-correlation functional is used instead. The present ordering of phases at 0 K can be calculated from PBE, and the energy difference between the two functionals is $\sim$1 meV; thus, the minor mismatch may be disregarded. The line density is the same in all geometries on the Γ-centered Monkhorst-Pack [53] K-mesh utilized for all DFT calculations. Each reciprocal lattice vector ($\overrightarrow{b_i}$)

TABLE I. DFT database used for features in input layers of the RANN potential. The RANN, which is only as precise as the training data, uses DFT approximations; therefore, convergence and consistency in DFT calculations are crucial for successful outcomes.

Sample description	Atoms per simulation	Number of simulation	Total atomic environment
Diamond cubic-Sn w/volumetric strains up to ±20%	8	99	792
β-Sn w/volumetric strains up to ±20%	4	98	392
BCT-Sn w/volumetric strains up to ±20%	2	98	196
BCC-Sn w/volumetric strains up to ±20%	2	99	198
SC-Sn w/volumetric strains up to ±20%	1	99	99
FCC-Sn w/volumetric strains up to ±20%	4	99	396
Diamond cubic-Sn w/shear strains up to ±5%	8	397	3176
β-Sn w/shear strains up to ±5%	4	600	2400
BCT-Sn w/shear strains up to ±5%	2	598	1196
BCC-Sn w/shear strains up to ±5%	2	598	1196
FCC-Sn w/shear strains up to ±5%	4	885	3540
α-Sn 2 × 2 × 2 orthogonal supercell w/strains up to ±5%	64	842	53 888
β-Sn 2 × 3 × 3 orthogonal supercell w/strains up to ±5%	72	854	61 488
BCT-Sn 3 × 3 × 3 orthogonal supercell w/strains up to ±5%	54	1000	54 000
BCC-Sn 3 × 3 × 3 orthogonal supercell w/strains up to ±5%	54	1000	54 000
FCC-Sn 3 × 2 × 2 orthogonal supercell w/strains up to ±5%	48	992	53 888
Diamond cubic-Sn decohesion energy	56	21	1176
β-[0 0 1]-Sn decohesion energy	20	21	420
β-[1 0 0] Sn decohesion energy	40	11	440
BCT-[0 0 1] Sn decohesion energy	20	21	420
BCT-[1 0 0] Sn decohesion energy	20	21	420
Diamond cubic-Sn [0 0 1] 1 × 1 × 6 free surface orthogonal supercell w/strains up to ±5%	48	500	24 000
β-Sn [0 0 1] 1 × 2 × 8 free surface orthogonal supercell w/strains up to ±5%	64	500	32 000
BCT-Sn [0 0 1] 2 × 2 × 8 free surface orthogonal supercell w/strains up to ±5%	64	500	32 000
BCT-Sn [1 0 0] 8 × 2 × 2 free surface orthogonal supercell w/strains up to ±5%	64	500	32 000
BCC-Sn [0 0 1] 2 × 2 × 8 free surface orthogonal supercell w/strains up to ±5%	48	489	31 296
β-Sn [0 0 1] 4 × 4 × 1 monolayer orthogonal supercell w/strains up to ±5%	64	250	16 000
BCT-Sn [0 0 1] 5 × 5 × 1 monolayer orthogonal supercell w/strains up to ±5%	50	106	32 000
BCC-Sn [0 0 1] 5 × 5 × 1 monolayer orthogonal supercell w/strains up to ±5%	50	500	31 296
β-Sn 2 × 3 × 3 trivacancy w/strains up to ±5%	69	400	27 600
BCT-Sn 3 × 3 × 3 trivacancy w/strains up to ±5%	51	155	7905
Amorphous structure	(66–95)	200	17 470
Isolate atom	1	1	1
Total		11 945	499 465

has a distance between its neighboring K-points of $2\pi \times 0.01$ Å^{-1}. The kinetic energy cutoff for all DFT calculations is set at 90 Ry, and 0.02 Ry is used as a Gaussian spreading for Brillouin-zone integration. Smearing of the Marzari-Vanderbilt [54] type is employed for every DFT computation.

RANN is trained using a database designed to replicate a wide range of distorted lattice structures, thermal perturbations, defects, free surfaces, and liquid structures. Table I summarizes the DFT training database. These include lattice distortions of up to 15% relative to equilibrium for the four allotropes studied here. To expand the possible applicability of the subsequent multistate MEAM [55], the database also includes nonobserved structures such as simple cubic (SC) and face-centered cubic (FCC). Most distorted structural data are contained inside the elastic domain, which allows for accurate prediction of the elastic behavior exhibited by pristine structures. The deformed data are produced as a result of hydrostatic volumetric compression and expansion of unit cells while preserving constant axial ratios, in addition to uniaxial deformation along the a, b, c axis with varying b/a and c/a ratios. In both cases, the network is aided in identifying the elastic response of the bulk structure by disrupting all degrees of freedom of cell vectors around the equilibrium state. Supercells of various sizes are generated, with atoms displaced from their relaxed ground-state position by a randomly generated vector within a cutoff distance ranging from 0.1 to 0.5 Å. This is done for the 72-atom $\beta(2 \times 3 \times 3)$, 54-atom BCT and BCC $(3 \times 3 \times 3)$, and 64-atom diamond cubic $(2 \times 2 \times 2)$ supercells to account for the effects of thermal perturbations. Also, each randomly perturbed structure was subjected to a small structural distortion of ±5% to determine the thermal expansion. Temperatures in the range ≈100–1200 K were sampled using these perturbations. The temperature of a given system was calculated by dividing the per-atom energy difference between the disturbed system and the ground state by the Boltzmann constant (k_B). Amorphous structures are added to the training database to better forecast behavior around the melting point and to accurately address liquid structures. Additionally, the training database consisted of free surfaces, vacancy clusters, and monolayers of various phases. A large database including a wide range of atomic configurations is necessary to ensure that the potential can predict behavior outside the training database. It will be shown below that the network can accurately predict some structures even if they were not included in the initial training set. The complete DFT dataset consists of ∼12 K structures with a total of ∼5 M atom environments.

B. RANN with EAM screening

The potential is generated using a multilayer perceptron artificial neural network, in accordance with the work of Dickel *et al.* [45]. In RANN, the input layer is a structural fingerprint describing the local atomic environment of a single atom, and the output layer is a prediction of the energy of that atom. This structure is like the neural network and descriptors of Behler and Parinello [56], with descriptors maintaining translational, rotational, and permutation invariance but with a different form. How the atomic configurations or the input to the network is presented has a significant impact on the accuracy and dependability of potentials based on artificial neural networks. To make the potential more physically motivated, a structural fingerprint of the local atomic environment is developed using the MEAM formalism. The final layer of the neural network consists of N atoms, each of which has its own unique energy that is determined by the surrounding environment. Following the first layer, the values for each subsequent layer, denoted by $\mathbf{A}^n$, are determined by the combination of the preceding layer as well as the weight and bias matrices denoted by $\mathbf{W}^n$ and $\mathbf{B}^n$ as follows:

$$Z^n_{l_n} = \sum_{l_n-1} W^n_{l_n l_n-1} A^{n-1}_{l_n-1} + B^n_{l_n}, \tag{2.1}$$

$$A^n_{l_n} = g^n\big(Z^n_{l_n}\big). \tag{2.2}$$

In this equation, l_n represents the total number of neurons in layer n, and $g^n(x)$ represents a nonlinear activation function. The fingerprint of the local atomic on its own structural fingerprint provides the input layer $\mathbf{A}^0$. Therefore, $\mathbf{W}^N$ is always a row vector, and $\mathbf{B}^N$ is always a single value, because there will only ever be a single node (representing the energy) in the output layer Z. The final bias $\mathbf{B}^N$ in Eq. (2.2) represents the target energy of the DFT database. The RANN fingerprint style is inspired by MEAM formalization, with angular screening added. This approach considers two distinct types of input fingerprints. First, simple pair interactions are analyzed and aggregated across all neighbors of an atom . A set of pair potential interactions of the form can be defined as follows for a given atom designated i:

$$F_n = \sum_{j\neq i} \left(\frac{r_{ij}}{r_e}\right)^n \exp^{\left(-\alpha_n \frac{r_{ij}}{r_e}\right)} \left(\frac{r_c - r_{ij}}{\Delta r}\right) S_{ij}. \tag{2.3}$$

Here, j and k label all the neighbor atoms of i within a cutoff radius r_c. For each pair of fingerprint contributions, n is a unique number, r_e is the equilibrium closest neighbor distance, S_{ij} is an angular screening term, and α_n are metaparameters that can be adjusted to improve the efficiency of the potential . In this paper, n is taken as $\in -1\ldots 3$ giving five 2-body terms. The MEAM potential parameter α is computed as a function of the ground-state values of the bulk modulus B_0, cohesive energy E_c, and the equilibrium atomic volume Ω_0 using the formula:

$$\alpha = \sqrt{\frac{9B_0\Omega_0}{E_c}}.$$

Using the first-principles data, α is calculated as 5.157041. All other metaparameters are given in Table II. The second type of fingerprint function considers three body terms with a shape comparable with partial electron concentrations in MEAM:

$$G_{m,p} = \sum_{j,k} \cos^m \theta_{jik} \exp^{\left(-\beta_p \frac{r_{ij}+r_{ik}}{r_e}\right)} f_c\left(\frac{r_c - r_{ij}}{\Delta r}\right) \times f_c\left(\frac{r_c - r_{ik}}{\Delta r}\right) S_{ij} S_{ik}, \tag{2.4}$$

where θ_{jik} is the angle between r_{ij} and r_{ik}, m is a positive integer, and β_p is a set of metaparameters that control the length scale of the various terms. Each RANN potential has a predetermined fingerprint based on the number and size of its hidden layers, as well as the weight, bias matrices, and activation functions of its individual layers. These activation functions have been employed for the potentials considered here:

$$g^n(x) = \frac{x}{10} + \frac{9}{10}\log\left(e^x + 1\right) \quad \text{for } n < N. \tag{2.5}$$

An alternative approach that avoids the unphysical outcomes is angular screening, in which the presence of an atom between two others reduces or eliminates the effective contact between them. MEAM has used a similar technique, and it has been used here for the screening process as well [57]. In a nutshell, the screening between two atoms is calculated as the sum of all the screening interactions involving atoms close by:

$$S_{ij} = \prod_{k\neq i,j} S_{ikj}, \tag{2.6}$$

where S_{ikj} is found by constructing a geometric ellipse with the three atoms, using $r_{i,j}$ as one of the axes. As a result,

TABLE II. Meta parameters.

Variable parameters	m	n	r_e(Å)	α	β_p	r_c(Å)	Δr
Values	$\in \{0\ldots 6\}$	$\in \{-1\ldots 3\}$	3.064190	5.157041	1,2,6,9	8.0	$r_c - r_e$

the formula for the screening parameter C_{ikj} can be written as follows:

$$C_{ikj} = 1 + 2\frac{r_{ij}^2 r_{ik}^2 + r_{ij}^2 r_{jk}^2 - r_{ij}^4}{r_{ij}^4 - \left(r_{ik}^2 - r_{jk}^2\right)^2},$$

and screening value

$$S_{ikj} = f_c\left(\frac{C_{ikj} - C_{\min}}{C_{\max} - C_{\min}}\right). \tag{2.7}$$

where $C_{\max}$ and $C_{\min}$ are metaparameters that can be adjusted to determine which neighbors can be omitted from calculations. The effect of including angular screening can be demonstrated by observing the modification of a single fingerprint as the length scale is continuously altered. In the absence of angular screening, the fingerprint value will fluctuate rapidly as new neighbors enter the radial screening distance at specific values of the lattice constant. If angular screening is incorporated with metaparameters such that, for instance, only the third NNs are ever included regardless of lattice parameter, the value variation is more gradual. The metaparameters used in potential construction are as follows.

With 33 features utilized to create the structural fingerprint, the whole network architecture can be represented as 33 × 21 × 1. One of the most significant issues for machine learned interatomic potentials is extrapolation outside of the training database. Because of the large potential configuration space, it is difficult, if not impossible, for the database to span all of it. Pun *et al.* [58] proposed physically informed neural networks whose structure was motivated by existing empirical formalisms to improve transferability and stability outside of the training data. Here, we employ a simple empirical potential as a lower bound on the energy. Through the use of the final activation function, the neural network contribution to the energy is required to be positive, thus improving stability over the entire configurational space. While predicted energies can still be arbitrarily large far from the training data, these regions will be automatically avoided in normal energy-conserving or temperature-controlled dynamic simulation assuming a low-energy initial configuration. For this potential, a bounding equation of state based on the EAM was employed. The energy predicted for a particular atom i can thus be written as

$$E_i = E_{\mathrm{EAM}} + E_{\mathrm{RANN}}, \tag{2.8}$$

where E_{EAM} is the energy determined by the empirical EAM potential, and E_{RANN} is the neural network prediction. The same empirical energy contribution is subtracted from the database targets so the neural network seeks to fit the difference between the EAM prediction and the DFT energy. The EAM style potential used is exactly equivalent to a MEAM potential with the angular partial electron densities set identically to zero ($t_1 = t_2 = t_3 = 0$). A complete description of the MEAM formalism can be found, for example, in Lee *et al.* [26]. The parameters describing the EAM state equation are given in Table III. These parameters are chosen using the following procedure. First, DFT results for the energy vs volume curve for a chosen reference state (in this case, a BCC structure) are reproduced using the parameters r_e, E_c, and α. Then the energy vs volume curve for a second structure with different coordination is reproduced by changing β_0, A_{sub}, and the screening parameters $C_{\min}$ and $C_{\max}$. Because the NN contribution is positive definite, the EAM baseline is then shifted down by increasing E_c and decreasing α until all of the training data are at least 0.5 eV above the baseline potential. This allows the baseline to bound all of the existing DFT data from below, so that the RANN potential can still correctly predict all of their energies. A smoothed ReLU function is used in the final RANN layer to ensure the neural network contribution to the energy is positive:

TABLE III. EAM potential parameters.

Variable parameters	Values	Variable parameters	Values
r_e	3.41	r_c	8.0
Δr	1.0	α	4.4
E_c	3.548	Reference structure	FCC
β_0	3.0	A_{sub}	1.4
$C_{\max}$	2.8	$C_{\min}$	0.4

$$g^N(x) = \log(e^x + 1). \tag{2.9}$$

The addition of these equations of state has been found to greatly increase the stability of the developed potentials for structures and temperatures well outside of the training data. At worst, the predicted energy will be the same as that of the EAM potential, a formalism which is known to show excellent transferability.When the network is being trained, 10% of the data is removed from each training batch at random and used afterwards for validation. The projected value of the output layer is compared with the measured energy obtained through DFT. Weights are updated to minimize the error function, also known as the loss function. The network is trained using the Levenberg -Marquardt (LM) algorithm [59,60]. When compared with gradient descent approaches, this one has been demonstrated to be more efficient at reducing the loss function. By incorporating a regularizer into the loss function, overfitting can be mitigated and boost model efficiency:

$$J(W^{[1]}, B^{[1]}, \dots W^{[L]}, W^{[L]}) = \frac{1}{m}\sum_{i=1}^{m} L[\hat{Y}^{(i)}, Y^{(i)}] + \frac{\lambda}{2m}\sum_{i=1}^{L} \|W^L\|_F^2. \tag{2.10}$$

The loss function is denoted by L, while the regularization parameter is denoted by λ. The mean squared error difference between the predictions from the output layer ($\hat{Y}$) and the known outputs (Y) from the database is the value that is used in the loss function L. In this case, the letter F indicates the addition of a Frobenius norm to the matrix, which is identical to adding the squared norm to the matrix. With the aid of the regularizer, it can be ensured that the magnitude of the weights remains low. The regularizer parameter λ is set to the value 10^{-4}. The regularization impact is diminished for smaller values of λ, while it is amplified for bigger weights. Here, root mean square error (RMSE) values for the training set are 1.713 meV/atom, while the validation set is 2.490 meV/atom. The RMSE value characterizes the last-epoch mean square

TABLE IV. RMSE and computational speed test for various RANN models, in comparison with the MEAM(Ko) potential. Note, all physics-based models include angular screening.

Model					RMSE				Relative computational	RANN energy
Physics-based		RANN			Energy (meV/atom)		Force	Stable	speed using	contribution
Model type	Screening	Included	M	Screening	Data base	Validation	(ev/Å)	potential	LAMMPS	(eV/atom)
None	—	Yes	7	Radial	6.1	6.5	2.51	No	22	2.7
				Angular	5.2	5.3	2.08		29	
Pair potential	Angular	No	—	Angular	—	28.9	0.78	Yes	0.05	—
		Yes	7		4	4.2	0.67		8	0.9
EAM		No	—		—	9.1	0.87		0.14	—
		Yes	3		2.8	4.1	0.06		14	
			7		2.1	2.6	0.06		20	0.6
MEAM (Ko)		No	—		—	6.6	0.17		1	—

error of convergence in training and validation. This suggests that the potential is not overfit since the validation set is so accurate, and the degree of precision is expected to hold true across all of the structures represented in the dataset. Since DFT is in significant disagreement with experiment, this energy is adjusted here to reproduce the experimental cohesive energy of α-Sn.

III. RESULTS

A. RANN potential selection

It was found that adding an underlying physics model to RANN improved the accuracy, stability, and transferability of the resultant potential. Table IV shows that the RANN energy database validation using only RANN is about on par with MEAM. However, the MEAM potential predicts the database forces much better than RANN. By using angular screening rather than radial screening, the fit produced by RANN is slightly improved at a small increase in computational time. Even though MEAM is over a factor of 20 times faster than RANN, it cannot represent the high-pressure phases as well as RANN. Specifically, the MEAM potential was found to be stable for a large number of our test simulations; however, it is shown below that it is unstable under dynamic shock loading. These results also show that including an underlying physical-based model leads to a lower overall energy input to the model from RANN, in addition to producing a better fit and validation. EAM and pair potential are considerably faster than MEAM or RANN with EAM, but they are not nearly as accurate or predictive as MEAM or RANN with EAM. RANN plus EAM requires more time to run, but the results are more accurate and reliable. Most importantly, the RANN potentials plus a pair potential or EAM physical model produce a potential that is stable for all phases. In this paper, the RANN plus an EAM physical model has been selected. We vary the size of the input fingerprint by varying the highest degree of the exponent m on the angular term in $G_{m,p}$, such that $m \in (0, 1, 2, \ldots, M-1)$, and the number of different β_p such that $p \in (1, 2, 3, \ldots, P)$, so that the total number of three-body fingerprints is $M \times P$. The value of M has been set to 7, as the reduction in the amount of computer time by using $M = 3$ was deemed not significant enough to justify the loss of accuracy. Other users may discover that the choice between the computational time and the degree of accuracy leads them to prefer a RANN potential that is less precise but faster. In the RANN GitHub repository, one can find both the RANN potential ($M = 3$, $M = 7$) as well as the DFT database and the LAMMPS version.

B. Fundamental material properties

Figure 2 shows an energy vs volume plot for diamond cubic, β, BCT, BCC, and FCC Sn determined by MEAM(Ko), EAM-R, and DFT. For a reasonable range of volume contraction and expansion, the curve remains smooth. As compared with MEAM potentials, the present potential provides closer agreement to DFT results. It is worth noting that, by including the screening function, the potential can be reliably extrapolated to arbitrarily large strains. A training point consisting of a single isolated atom is added to the database, as was mentioned earlier. For the EAM-R potential to obtain the correct cohesive energy and interpolate correctly to the isolated state, this piece of information is crucial.

Table V shows several 0 K mechanical properties for the four experimentally observed phases of Sn, including

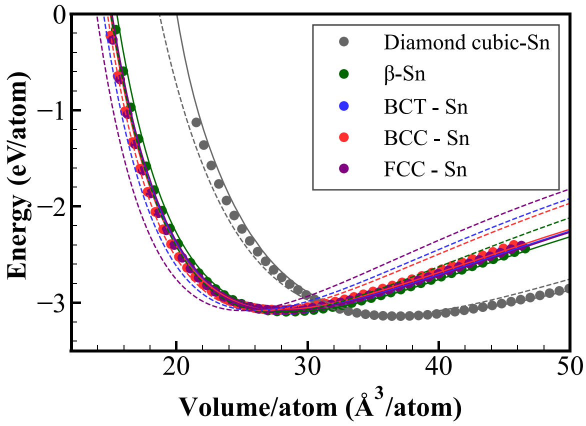

FIG. 2. Equation of state for various phases of Sn. The dashed and solid lines are from MEAM(Ko) and EAM-R potentials respectively. All DFT calculations (points) are from the current database.

TABLE V. Fundamental material properties for different phases (diamond cubic, β, BCT, and BCC) of Sn: Equilibrium volume Ω (Å^3/atom), cohesive energy E_c (eV), lattice parameter a, c (Å), c/a ratio, bulk modulus B_0 (GPa), elastic modulus $C_{11}, C_{12}, C_{13}, C_{33}, C_{44}$ (GPa), structural energy differences ΔE (eV/atom), surface energy (mJ/m^2), and vacancy formation energy (eV) as computed by present DFT, MEAM(Ko), and EAM-R potentials as well as available experimental data.

Properties	Experiment	DFT	MEAM(Ko)	EAM-R
		Diamond cubic		
Ω	34.059 [62]	36.893	35.628	36.846
E_c	3.140 [63]	3.548	3.135	3.140
a (Å)	6.483 [62]	6.658	6.581	6.655
B	42.6 [64]	35.175	40.578	35.327
C_{11}	69.1 [64]	52.725	50.413	53.967
C_{12}	21.3 [64]	29.819	35.660	26.006
C_{44}	42.6 [64]	22.541	10.531	20.974
$\Delta E_{\alpha\to\beta}$		0.046	0.033	0.046
$\Delta E_{\alpha\to\gamma}$		0.0623	0.053	0.062
$\Delta E_{\alpha\to\delta}$		0.068	0.053	0.068
$\Delta E_{\alpha\to\text{fcc}}$		0.0617	0.052	0.0613
$\Delta E_{\alpha\to\text{fcc}}$		0.061	0.050	0.060
$E_{\text{surf}}^{(001)}$		688.144	567.099	614.956
E_f^{vac}		0.917	1.055	0.944
		β		
Ω	27.064 [62]	28.361	27.512	28.466
E_c	3.10 [4]	3.502	3.102	3.094
a	5.831 [62]	5.909	5.859	5.924
c	3.184 [62]	3.249	3.206	3.245
c/a	0.546 [62]	0.549	0.547	0.548
B	57.0 [62]	46.713	57.137	46.733
C_{11}	73.2 [62]	68.544	89.737	59.089
C_{12}	59.8 [62]	57.846	46.683	53.246
C_{13}	39.1 [62]	32.865	36.915	30.705
C_{33}	90.6 [62]	89.121	93.729	73.102
C_{44}	21.9 [62]	21.928	7.901	15.598
$E_{\text{surf}}^{(001)}$		401.341	393.127	409.622
$E_{\text{surf}}^{(100)}$		322.329	345.358	294.673
E_f^{vac}		0.738	0.848	0.741
		BCT		
Ω	23.068 [15]	27.772	25.921	27.855
E_c		3.486	3.082	3.078
a (Å)	3.70 [15]	4.030	3.906	4.040
c (Å)	3.37 [15]	3.419	3.397	3.413
c/a	0.911 [15]	0.848	0.869	0.845
B	63 [65]	48.312	64.509	48.530
C_{11}		56.431	89.805	46.175
C_{12}		34.385	64.774	42.540
C_{13}		49.146	49.459	47.509
C_{33}		74.685	73.587	69.307
C_{44}		11.324	42.517	14.748
$E_{\text{surf}}^{(001)}$		371.696	443.472	357.188
$E_{\text{surf}}^{(100)}$		347.132	467.849	332.066
E_f^{vac}		0.434	0.352	0.426
		BCC		
Ω	24.5 [65]	27.588	26.415	27.619
E_c		3.480	3.082	3.072
a (Å)	3.659 [65]	3.807	3.752	3.808
B	92 [65]	49.145	63.264	51.441
C_{11}		343.357	73.187	45.154
C_{12}		51.319	58.303	54.585
C_{44}		28.626	26.269	28.652
$E_{\text{surf}}^{(100)}$		424.572	480.410	434.476
E_f^{vac}		0.556	0.425	0.519

cohesive energy, lattice parameter, and elastic constants, surface, and vacancy formation energies as predicted by the EAM-R potential in comparison with DFT and MEAM(Ko) potential. It should be noted that the DFT prediction for the lattice constant is 1.3% higher than that observed experimentally. Consequently, the predicted values from EAM-R are comparable with those measured experimentally. MEAM(Ko) potential is optimized for the β-Sn phase, which reproduces the properties for that phase only, whereas EAM-R agrees well with the DFT reference values for all four phases. All DFT results are obtained from the current calculations, which demonstrates a high degree of agreement with other DFT computations [61] utilizing the GGA pseudopotential.

In addition to the properties that are derived directly from structures and energy in the training set, Table V shows some properties such as free surface and vacancy formation energy. Examining such structures provides some insights into the extent that a potential is transferable to unidentified atomic surroundings. It is important to note that the potential is not trained to relaxed free surfaces or monovacancies in numerous phases, both of which are accurately predicted by EAM-R. Due to the excellent agreement of this potential with DFT, it is possible to explore atomic-scale physical and chemical processes such as fracture and crystal formation. Figure 3 displays the relative error to DFT of a variety of material properties, including those in Table V, computed from EAM-R, as well as the properties obtained from the MEAM(Ko) potential. Here, the relative deviation vs DFT-computed properties is displayed rather than the actual properties themselves. The EAM-R predictions are, for all phases, in better agreement with DFT than the MEAM(Ko) predictions. Typically, the deviation in properties for all four phases in EAM-R potential is ±8% or less. Further, EAM-R deviates from DFT by no more than 11% for all material properties.

C. Force validation

In EAM-R, forces are computed by direct differentiation of the EAM-R equation, and *ab initio* calculations are used to determine the forces acting on individual atoms ($\mathbf{f}_i = -\partial E/\partial \mathbf{r}_i$). Indeed, forces calculated from DFT are extremely useful training data for a ML model, allowing one to train on both energy and force data at a cost similar to training on the energy data alone. Here, EAM-R is trained solely using energies from DFT, leading to RMSE values of 0.070, 0.051, 0.026, and 0.029 eV/Å for the diamond cubic, β, BCT, and BCC-Sn forces, respectively. The x, y, and z force components for

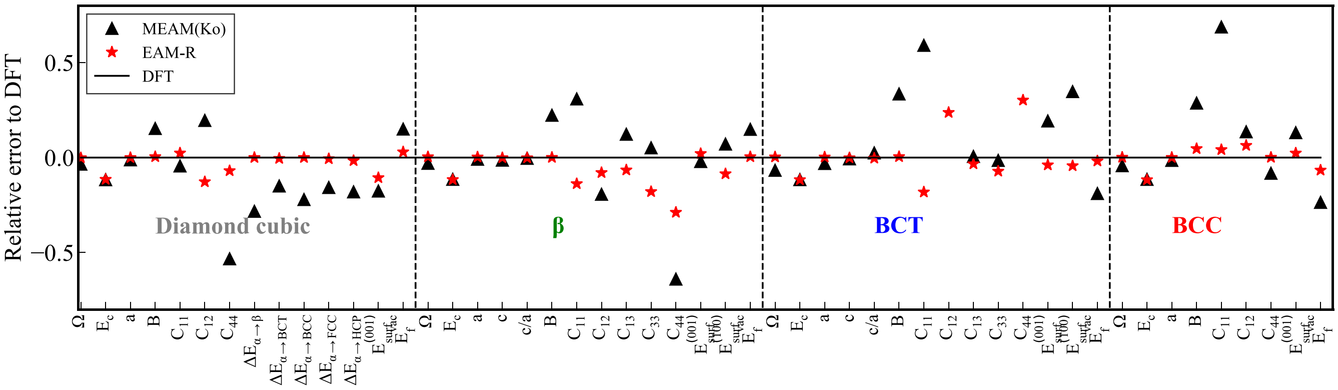

FIG. 3. Relative errors in material properties for MEAM(Ko) and EAM-R potentials compared with DFT shown in Table V.

randomly perturbed diamond cubic, β, BCT, and BCC are shown in Fig. 4. The excellent match between the predicted vs calculated forces demonstrates that EAM-R is likely to be successful in dynamic predictions of the kinetics of Sn structures. Forces have been reported to have an RMSE of 0.097 eV/Å when using the MEAM(Ko) potential [25] fitting to their DFT database. While the empirical potential is adequate for fitting forces, the ML potential here provides a more accurate match to DFT forces. For comparison, for BCC transition materials, the RMSE for the Gaussian approximation potential was 0.04 eV/Å [66], and the spectral neighbor analysis potential value was 0.14 eV/Å [67].

D. Decohesion energy

To determine that EAM-R is appropriate to study fracture, the energy vs separation distance for rigid separation between two blocks of materials has been explored. During loading, the crack-tip shape is determined by this decohesion curve [68]. Figure 5 shows the decohesion energy vs normal separation distance for (001) planes for various crystal structures using DFT, EAM-R, and MEAM(Ko) potentials. The DFT data were part of the training set. The energy at maximum separation is double that of the unrelaxed surface energy compared with completely relaxed surfaces in Table V. Prior to complete dissociation, EAM-R shows a small peak in energy which has a negligible impact and therefore is of little practical importance. Additionally, the results from EAM-R agree with DFT for all four phases of Sn. In contrast, the MEAM(Ko) potential only predicts the decohesion energy accurately for β-Sn. From this comparison, it may be concluded that EAM-R, in contrast with current state-of-the-art interatomic potentials, is capable of

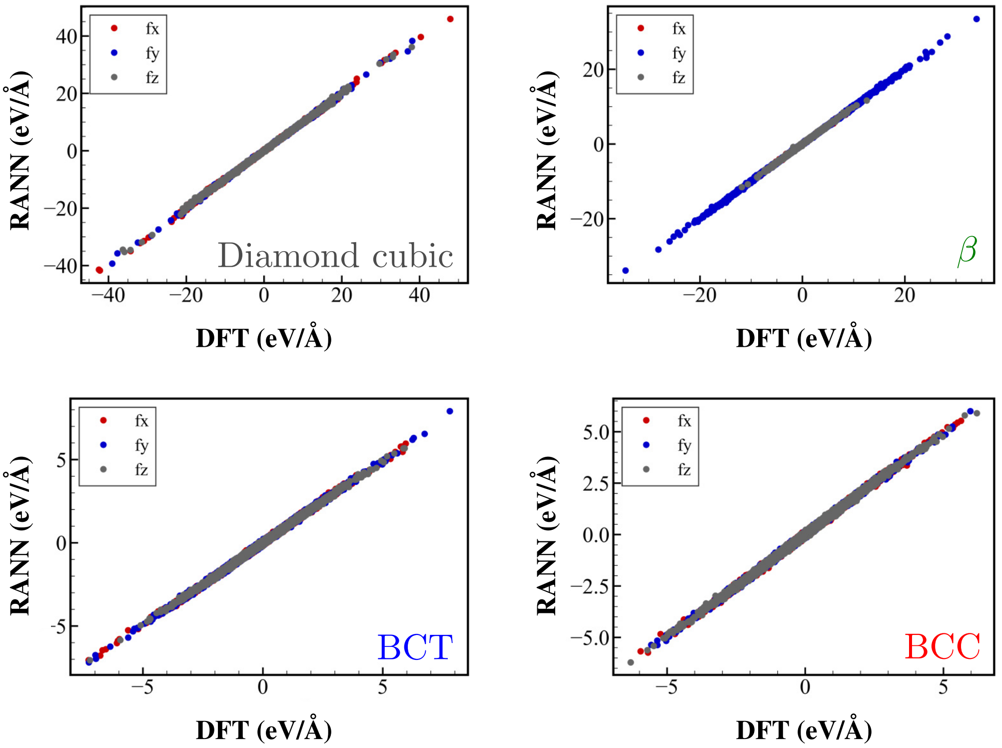

FIG. 4. Force vector comparison between DFT and the EAM-R potential for Sn for randomly perturbed supercells.

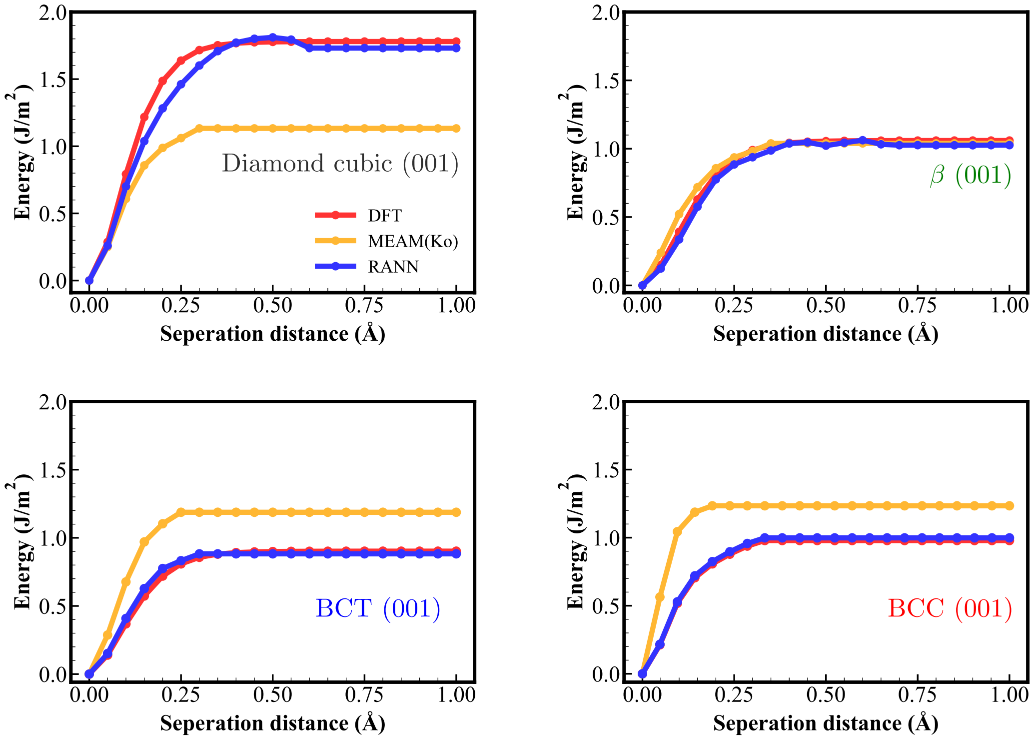

FIG. 5. Decohesion curves for (001) planes for different phases of Sn; a comparison of DFT, EAM-R, and MEAM(Ko) potentials. DFT data points are included in the training set.

accurately predicting fracture in the experimentally observed Sn allotropes.

E. Generalized stacking fault energy

Solder joint reliability, as shown by Yang and Li [69], is dependent on an adequate understanding of anisotropic mechanical behavior in β-Sn. Previous studies [70,71] have shown that the generalized stacking fault energy (GSFE) is critical in explaining dislocation properties and hence plasticity. Here, an evaluation of the ability of the EAM-R potential to predict the GSFE in β-Sn allows for determining the likelihood of successful prediction of plastic deformation in Sn. As shown by experimental studies by Telang and Bieler [72] and first-principles computations by Bhatia *et al.* [73], the $\{1\,0\,0\}\,\langle 0\,0\,1\rangle$ slip system is the easiest to activate. GSFEs are calculated for a few of the distinct slip systems to show how the current potential represents the deformation behavior of Sn and are shown in Fig. 6. A comparison of the unstable fault energy (USFE) using EAM-R (0.0178, 0.018, 0.017) eV/Å^2 and MEAM(Ko) (0.0393, 0.0236, 0.045) eV/Å^2 with the results from prior *ab initio* calculations by Bhatia *et al.* [73] reveals that the USFE calculated from EAM-R for the $(1\,0\,0)[0\,0\,1]$, $(1\,0\,0)[0\,1\,0]$, and $(1\,1\,0)[0\,0\,1]$ slip systems are in good match with the DFT data (0.0124, 0.0146, and 0.0134 eV/Å^2). It is important to note that the training database did not include any information about stacking faults. In contrast to the most accurate Sn potential in the literature, EAM-R will most probably lead to the discovery of dislocation dissociation reactions, such as those that simulate individual dislocation cores or noncollinear dissociations at the atomic scale.

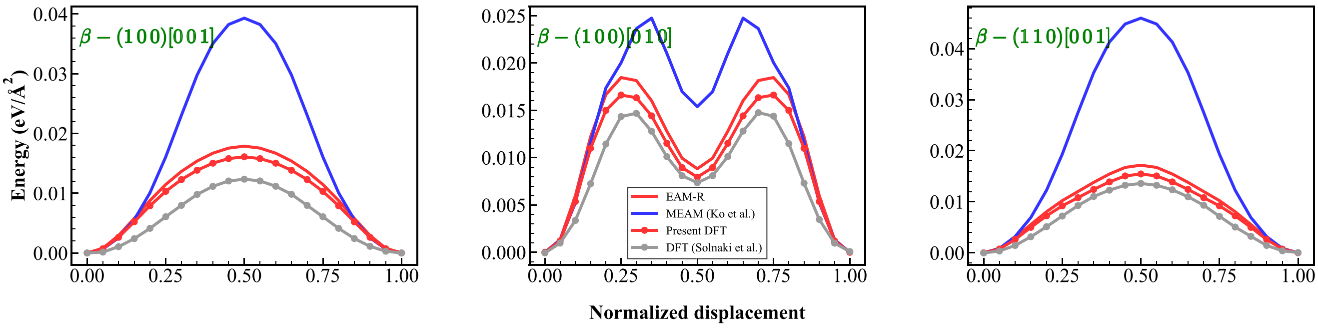

FIG. 6. Stacking fault energies for β-Sn for different slip systems. The DFT results are from Bhatia *et al.* [73] as well as this paper. These DFT results are not included in the training set; hence, the stacking fault energies are predictions of the EAM-R potential.

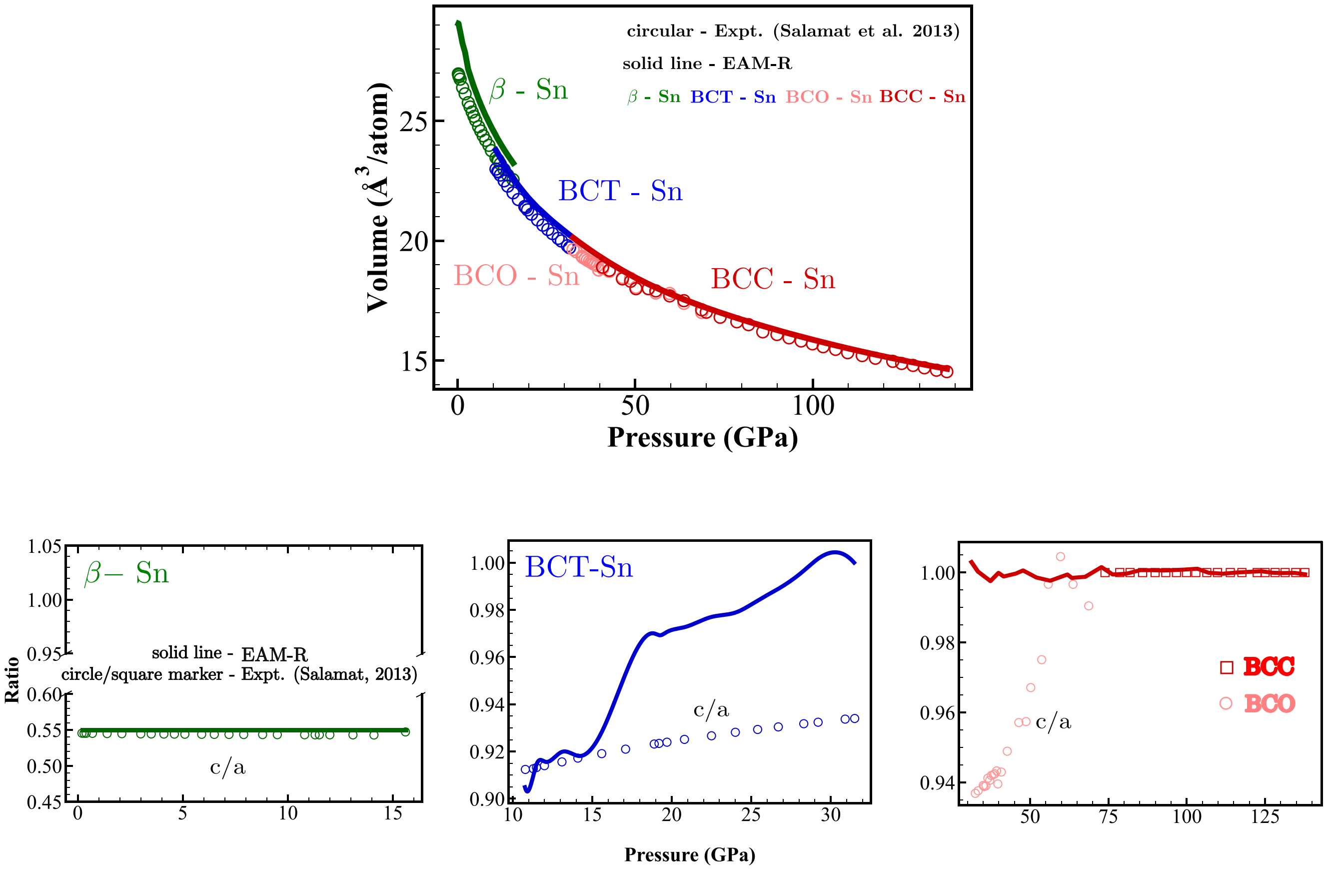

FIG. 7. High-pressure phases of Sn at room temperature: a comparison between experiments [65] and EAM-R for pressure-volume and lattice constant ratios over a wide pressure range. The c/a ratio is denoted by circles (expt.) and solid lines (EAM-R). Here, 300 K MD simulation results are compared with room temperature experimental data.

F. Multiphase prediction of Sn

Structural transformations at high pressure

Here, β-Sn undergoes a pressure-induced phase transition from the BCT to the BCC structure. Liu and Liu [16] found coexistence of both crystalline forms between 9.7 ± 1 GPa and 11.1 ± 8 GPa, and later research found this coexistence to be true over a wider pressure range [65]. Salamat *et al.* [65] observed a metastable two-phase structure up to 15.7 GPa. Comparing the β-Sn and BCT phases at 10.8 GPa, the volume decrease is $\sim$2%. In earlier investigations, it was thought that the BCT-Sn phase would eventually transform into a BCC structure [11,16]. A recent study by Salamat *et al.* [65] found evidence for a first-order phase transition between the body-centered orthorhombic (BCO; $b/a = 0.996$) and BCC polymorphs. For our purposes, the BCO and BCC structures are degenerate in energy and may be considered the same structure. The BCT phase transforms into the BCO phase at 32 GPa. Starting at 40 GPa, a change to the BCC structure was found, though the BCO phase was detected at pressures as high as 70 GPa. This indicates that the BCC phase can transform into BCT or BCO by a straightforward and continuous lattice deformation in response to small deviations from hydrostatic pressure. The studies demonstrate unequivocally that the BCO and BCC diffraction signals can coexist across a large pressure range [74]. The author performed extensive research into the BCO phase using *ab initio* calculations and discovered that the global minimum remained centered at $b/a = 1$ for both tetragonal and cubic solutions across all pressures at 0 K.

A series of molecular dynamics (MD) simulations have been performed using LAMMPS [75] at 300 K utilizing the EAM-R potential to explore the structural evolution of the high-pressure phases of Sn. Using the pressure components of the stress tensor as the driving forces, bulk β-Sn is equilibrated in an anisotropic manner at different pressure regions (0.2–16 GPa) such that the x, y, and z dimensions can be separately controlled. Two diagonal components (x and y) of the pressure tensor are allowed to be coupled together, forcing tetragonal symmetry, in BCT-Sn from 10 to 32 GPa. All three dimensions of the BCT structure are allowed to relax after being equilibrated in an anisotropic fashion between 32 and 40 GPa. Beyond 40 GPa, the structure is forced to have cubic symmetry. Figure 7 demonstrates that the EAM-R pressure-volume curve is consistent with experimental data. The DFT volume for β-Sn is 3.4% higher at 0 K than experiments, and this disparity is the cause of the minor structural differences between EAM-R and experiment. Above 40 GPa, EAM-R predicts a stable BCC phase and fails to locate the observed BCO structure. EAM-R does this since it is trained directly through first-principles calculations, independent of experimental database. Not surprisingly, EAM-R also failed

TABLE VI. Thermal properties calculated using the EAM-R potential in comparison with experimental data and MEAM(Ko). The quantities represent the thermal expansion coefficient $\varepsilon(1/\mathrm{K})$, the heat capacity $C_p(\mathrm{J/mol\,K})$ at constant pressure, the melting temperature $T_m(\mathrm{K})$, the melting enthalpy $\Delta H_m(\mathrm{kJ/mol})$, and change in volume upon melting $\Delta V_m/V_{\mathrm{solid}}(\%)$.

Phase	Property	Pressure	Experiment	MEAM (Ko)	EAM-R
Diamond cubic	ε (300 K)	0 GPa		1.208×10^{-5}	3.47×10^{-5}
	C_p (300 K)			25	25
	T_m			328	455
	ΔH_m			7	8
	$\Delta V_m/V_{\mathrm{solid}}$			2	6
β	ε	0 GPa	2.35×10^{-5} [76]	1.86×10^{-5}	2.84×10^{-5}
	C_p		26.5 [77]	26	26
	T_m		505 [78]	368	525
	ΔH_m		7 [78]	3	8
	$\Delta V_m/V_{\mathrm{solid}}$		2.3 [78]	4	3
	ε	5 GPa		1.30×10^{-4}	1.53×10^{-5}
	C_p			33	26
	T_m			465	587
	ΔH_m			3	5
	$\Delta V_m/V_{\mathrm{solid}}$			1	1
BCT	ε	12 GPa		Not stable	4.27×10^{-5}
	C_p				24
	T_m				1198
	ΔH_m				11
	$\Delta V_m/V_{\mathrm{solid}}$				1
BCC	ε	40 GPa		Not stable	1.45×10^{-5}
	C_p				25
	T_m				1817
	ΔH_m				16
	$\Delta V_m/V_{\mathrm{solid}}$				2

to show a first-order phase transition between the two polymorphs (BCT and BCO) in the pressure range of 32–40 GPa, where both previous [65] and current DFT failed to detect any variation in the b/a ratio. Lattice constant ratios at room temperature vary across a wide pressure range, as depicted in Fig. 7. Although EAM-R predicts a $0.9 < c/a < 1$ ratio in the BCT phase from 11 to 32 GPa, the energy difference between the BCT and BCC phases is < 2 meV at 300 K, which is in agreement with prior DFT studies at 0 K. At room temperature, the predicted c/a ratio of the BCT structure shows a more rapid increase with pressure than experiments, yet a stable BCT phase is predicted, which is an improvement over any interatomic potential ever reported. Using the 0 K DFT as a guide, it appears that these small differences in lattice constant ratios are due to the inaccuracies in the DFT calculations, rather than the EAM-R fitting. However, DFT calculations at 300 K have not been performed, so this supposition must remain an assumption at this point.

By comparing several properties at finite temperatures, the transferability of EAM-R is further explored. Table VI shows how the thermal properties of various phases compare with experimental data and the MEAM(Ko) potential. MD simulations have been performed using an isobaric-isothermal (NPT) ensemble at the desired temperatures and pressures allowing for the determination of these properties. When comparing EAM-R with MEAM(Ko) for all properties of β-Sn, EAM-R provides better agreement with experiment. The results of calculations from EAM-R are presented for extreme pressures. In this paper, we also highlight the pressure-induced instability of the MEAM(Ko) potential. Increases in pressure render the BCT and BCC phases unstable using the MEAM(Ko) potential.

Figure 8 illustrates a typical snapshot of the equilibrated solid phases at 300 K using the EAM-R potential. A stable phase is maintained by equilibrating distinct phases at varying pressures. Diamond cubic crystal is shown in cyan, β structure that is SC is shown in purple, and BCT and BCC structures are shown in blue using the polyhedral template matching [79] in the OVITO software [80].

G. Phase diagram prediction using Gibbs free energy calculations

A homogenous transformation between any two solid phases is not favorable on the MD time scale due to the high-energy barrier between phases. The relative Gibbs free energy between phases determines the transition temperature between two phases. In accordance with the work of Dickel and Barrett [81], the Gibbs-Helmholtz equation may be used to calculate the relative free energy of any two phases given their enthalpy difference, the relative enthalpy, and free energy of a reference phase (in this case, liquid). To conduct this computation, the melting point of each phase was determined using a solid-liquid interface method [81], as depicted in Fig. 9. A supercell (233 600 atoms for α-Sn, 116 800 atoms for β-Sn, and 64 000 atoms for BCT and BCC) was built with

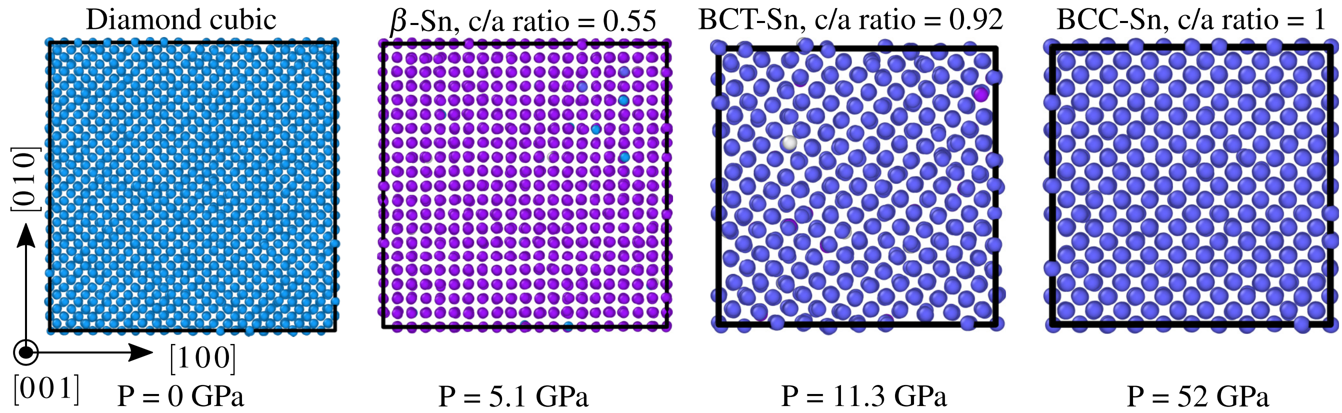

FIG. 8. Stable phases of Sn using the EAM-R potential at different pressures at 300 K.

half of the box having either the solid or liquid phase and the other half heated to above the melting point to form a liquid phase. The solid-liquid phase boundary is better defined with the aid of this supercell. Once the overall energy has been adjusted such that the system does not completely melt or solidify, it can evolve under constant enthalpy and pressure. It is possible for one phase to expand while the other contracts at the interface, but once the phases have equilibrated, the temperature will settle to its melting point. After the interface has stabilized, the average temperature and pressure are recorded by averaging over 1.2 ns of simulation time. The computed melting temperature of β-Sn at zero pressure is 525 K, which is in good agreement with experiments (505 K). To compute the melting point at different pressures, a similar approach is used with a smaller lattice constants to simulate greater pressures ranging from 0.5 to 137 GPa in increments of 5 GPa.

Once the melting temperatures of any pair of phases are known, their relative free energy may be computed by integrating the Gibbs-Helmholtz equation using the enthalpy as a function of temperature for both phases and the liquid phase:

$$\frac{1}{T}\Delta G = \frac{G(T_{\text{melt}})}{T_{\text{melt}}} + \int_{T}^{T_{\text{melt}}} \frac{H(T')}{T'^2} dT'. \tag{3.1}$$

The enthalpy $H(T)$ for a temperature range up to the melting point of that particular phase is computed by heating a periodic supercell of $10 \times 10 \times 10$ atoms to the necessary temperature and averaging the energy for 0.5 ns using an NPT ensemble. This method allows for precise calculation of the projected equilibrium phase transition temperatures but at a higher computing cost. The temperature at transition is determined by the sign shift in the relative free energy. Table VII provides an in-depth description of how the Gibbs free energy of a diamond cubic-β pair was calculated at atmospheric pressure.

Table VIII depicts the polynomial coefficient from the free energy calculation for each of the four solid and liquid phases. At the temperature range where the solid phase is observed at constant pressure ranging from 0 to 137 GPa (0.1 GPa pressure increment from 0 to 1, 2 GPa increment from 1 to 30, and 5 GPa pressure increment from 30 to 137 GPa), the free energy is estimated. The polynomial coefficients for various pressures are then fitted as a function of pressure. Figure 10 shows the calculated Sn phase diagram using EAM-R compared with experimental data. In the low-pressure region (left panel), it is demonstrated that the predicted diamond cubic-to-β monovariant line agrees well with the experimental data [82]. Experiments measure a transition temperature of 286 K,

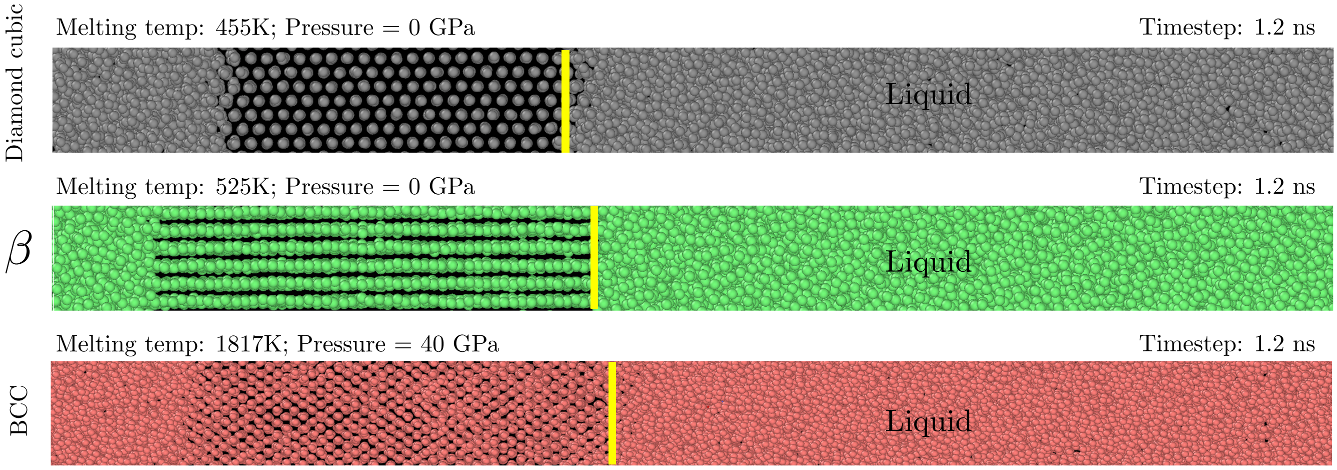

FIG. 9. Solid-liquid phase region for different phases using the EAM-R potential following the method by Dickel and Barrett [81]. For visualization purposes, only a few atomic layers are shown. The color of atoms corresponds to the color depicted in Fig. 1.

TABLE VII. Relative Gibbs free energy calculation for a sample phase pair.

Gibbs free energy	Transition temperature
- The relative free energy of the diamond cubic (α) and β phases at T is given by $\frac{1}{T}\Delta G = \int_{T}^{T_{melt,\alpha}} \frac{H_{\alpha}(T') - H_{\beta}(T')}{T'^2} dT' + \int_{T_{melt,\alpha}}^{T_{melt,\beta}} \frac{H_{liq}(T') - H_{\beta}(T')}{T'^2} dT'$ - At 0 pressure, quadratic coefficients of fitting enthalpy as a function of temperature for $(aT^2 + bT + c)$ of solid α, β and liquid phases are $5.31492e-09, 2.63501e-04, -3.14044$, $1.1847e-8, 0.00033, -3.12946$ and $8.621066e-08, 4.524903e-05, -2.88109$ respectively, and melting temperature $T_{melt,\alpha} = 454.45$ K and $T_{melt,\beta} = 524.846$ K.	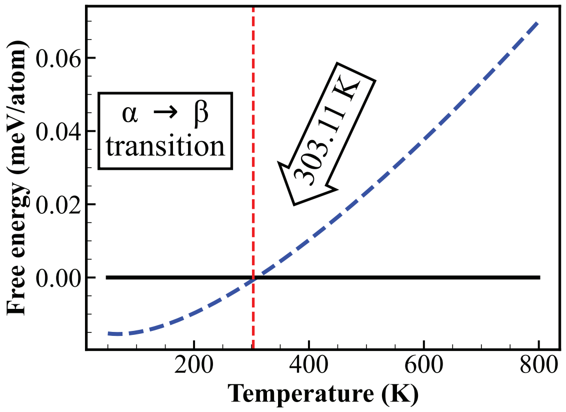

Plugging the coefficients in the free energy equation provides the transition temperature as follows:

$$\Delta G = T\int_{T}^{454.45} \frac{(5.31492e-09T^2 + 2.63501e-04T - 3.14044) - (1.1847e-8T^2 + 0.00033T - 3.12946)}{T^2} dT + \int_{454.45}^{524.846} \frac{(8.621066e-08T^2 + 4.524903e-05T - 2.88109) - (1.1847e-8T^2 + 0.00033T - 3.12946)}{T^2} dT$$

whereas EAM-R predicts a transition temperature of 303 K [1]. The melting point decreases with increasing pressure in agreement with the limited experimental data. The 0 K transition pressure is 0.96 GPa which agrees with our DFT database transition pressure of 0.73 GPa, which is also consistent with previous DFT calculation [83,84].

TABLE VIII. Fitting coefficients of free energy calculation as a function of pressure [H (eV/atom), P (GPa), T (K)].

$$H = a_G(P)T^2 + b_G(P)T + c_G(P)T$$
$$a_G(P) = a_{G'}(P)^2 + b_{G'}(P) + c_{G'}$$
$$b_G(P) = a_{G'}(P)^2 + b_{G'}(P) + c_{G'}$$
$$c_G(P) = a_{G'}(P)^2 + b_{G'}(P) + c_{G'}$$

Phase		$a_{G'}$	$b_{G'}$	$c_{G'}$
Diamond cubic	a_G	7.27384×10^{-10}	5.81100×10^{-10}	5.26229×10^{-9}
	b_G	5.56637×10^{-7}	4.61939×10^{-6}	2.63091×10^{-4}
	c_G	-6.25738×10^{-4}	2.28164×10^{-1}	-3.13996
β	a_G	-3.44776×10^{-11}	6.74505×10^{-10}	1.82585×10^{-8}
	b_G	-1.35706×10^{-8}	2.96024×10^{-7}	3.27690×10^{-4}
	c_G	-1.43342×10^{-3}	1.80486×10^{-1}	-3.11088
Liquid	a_G	-6.78697×10^{-13}	-3.25029×10^{-12}	4.20308×10^{-8}
	b_G	1.88913×10^{-9}	1.37557×10^{-8}	3.94103×10^{-4}
	c_G	-1.04849×10^{-3}	2.25179×10^{-1}	-3.31286
BCT	a_G	7.08012×10^{-11}	2.36660×10^{-9}	5.37182×10^{-8}
	b_G	-1.55407×10^{-8}	-1.27407×10^{-7}	2.74013×10^{-4}
	c_G	-6.42055×10^{-4}	1.62640×10^{-1}	-3.05045
BCC	a_G	-2.14347×10^{-12}	5.76210×10^{-11}	2.27222×10^{-8}
	b_G	8.45428×10^{-10}	1.74316×10^{-9}	2.47438×10^{-4}
	c_G	-1.37657×10^{-4}	1.27785×10^{-1}	-2.36166

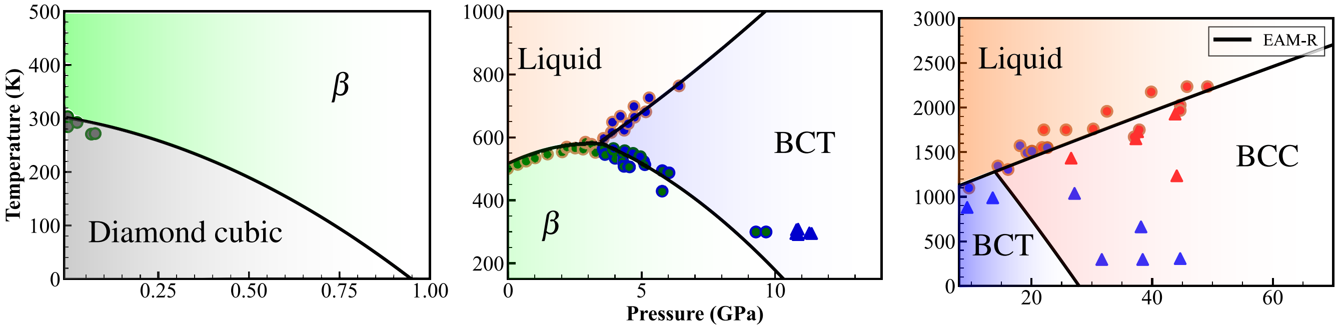

FIG. 10. The Sn phase diagram. The solid line is derived directly from the equation for relative free energy. The gray, green, blue, red, and orange colors correspondingly depict the diamond cubic, β, BCT, and liquid phases. The same color scheme was used for the markers. The triangles indicate the stable phase for the given temperature and pressure. The liquid coexistence points were derived from the calculations needed to get the Gibbs free energy reference melting point. A wide range of experiment provides the bicolor circle indicators of the phase boundary diamond cubic-β [82,92], β-liquid [93–96], β-BCT [11,16,86,94,97–100], solid-BCT (blue triangle) [11,65,86,101,102], BCT-liquid [94,97,98,100], solid-BCC (red triangle) [91], and BCC-liquid [87–89].

As pressure increases (center panel), EAM-R predicted the β-BCT-liquid triple point to be 576.2 K and 3 GPa, whereas the experimental observation is 588 K and 2.8 GPa. The differences between EAM-R and the experimental observation are 12 K and 0.2 GPa, respectively. The predicted pressure for the β-to-BCT phase transition at 300 K is 8.9 GPa, which is in excellent agreement with previous investigations indicating a transition pressure ranging from 8.3 to 9.3 GPa [16,74,85,86]. The predicted β-BCT monovariant line agrees well with experiments near the triple point. At 0 K, the transition pressure is 10.5 GPa, which is in excellent agreement with the DFT database value of 12 GPa [83]. The predicted melting point of BCT increases with increasing pressure in excellent agreement with experiment. The predicted liquidus of β agrees nicely with experiment, reflecting the ~12 K difference seen in the triple point and ~20 K at zero pressure melting point of β. A minor disagreement emerges between EAM-R and the experimental results close to the BCT-BCC-liquid triple point (right panel), which is calculated to be 1287 K and 11.2 GPa but experimentally observed to be 1515–1587 K and 18–21 GPa [74,87–89]. Both the BCT and BCC liquidus predictions are in good agreement with experiment. EAM-R underestimates the BCT-to-BCC transition pressure. Since Sn is highly metastable in this regime, the results are carefully studied in relation to the BCT-BCC phase transition. At room temperature, the transition pressure from BCT to BCC is calculated to be 31.5 GPa compared with the pressure of 41.2 ± 8.4 GPa determined from experimental measurements. At 0 K, EAM-R predicts a transition pressure of 26.7 GPa, while the DFT calculations yield 27.6 GPa [74], and experiments extrapolate to ~45 GPa [90]. It appears that the error in EAM-R stems from the error in DFT and not in the EAM-R fit. In addition to the pressure-temperature points at the boundary, a couple of experimental points (marked with a triangle) that are stable in this particular region [16,65,91] are depicted in Fig. 10.

IV. DEFORMATION BEHAVIOR OF Sn UNDER HIGH STRAIN RATE LOADING

To understand the mechanical stability of the various phases of Sn under high strain rate loading, MD simulations using LAMMPS were performed. A pure Sn single crystal with dimensions $lx = 17.73$ nm, $ly = 17.73$ nm, $lz = 17.87$ nm for the β-Sn phase (198 000 atoms) and $lx = 20.15$ nm, $ly = 20.15$ nm, $lz = 20.15$ nm (250 000 atoms) for the BCC phase was created. Next, a spherical nanovoid with a 2.4-nm diameter is created in the simulation box by removing ~0.1% of the atoms. The system is then relaxed by minimization of energy, followed by equilibration at constant pressure (4 GPa for β and 60 GPa for BCC) and temperature (NPT) at $T = 300$ K. This condition was chosen because, according to experimental studies, these phases are stable under these conditions. A 1-fs timestep is utilized in these simulations. All three directions have periodic boundary conditions applied. Finally, a uniaxial compression deformation at a constant strain rate of 10^9/s is performed. The spherical void is added in the cell to facilitate dislocation nucleation and to determine whether the potential is optimal for studying the high strain rate deformation behavior of Sn. Figure 11 demonstrates that, at peak stress, the β-Sn structure was stable with dislocations nucleating from the free surface of the void. The purple color shows the diamond cubic structure as determined by the polyhedral template matching. In the case of the MEAM(Ko) potential, the structure is not found to be stable, as the β-Sn structure could not be maintained; instead, polyhedral template matching indicates that a low-energy HCP structure is formed. When BCC is compressed to a pressure of 60 GPa, EAM-R retains the BCC structure (shown by blue atoms from polyhedral template matching), whereas MEAM(Ko) again transforms into an HCP structure. This finding clearly indicates that the EAM-R potential can properly predict the propagation, slip, and general dynamical behavior of dislocations in pure Sn at high pressure. Shock compression of pure Sn at high pressure is a subject of an upcoming publication.

V. CONCLUSIONS

In this paper, we have developed a hybrid potential that combines the conventional EAM with a ML approach. Essentially, the ML component of the potential is an additional term

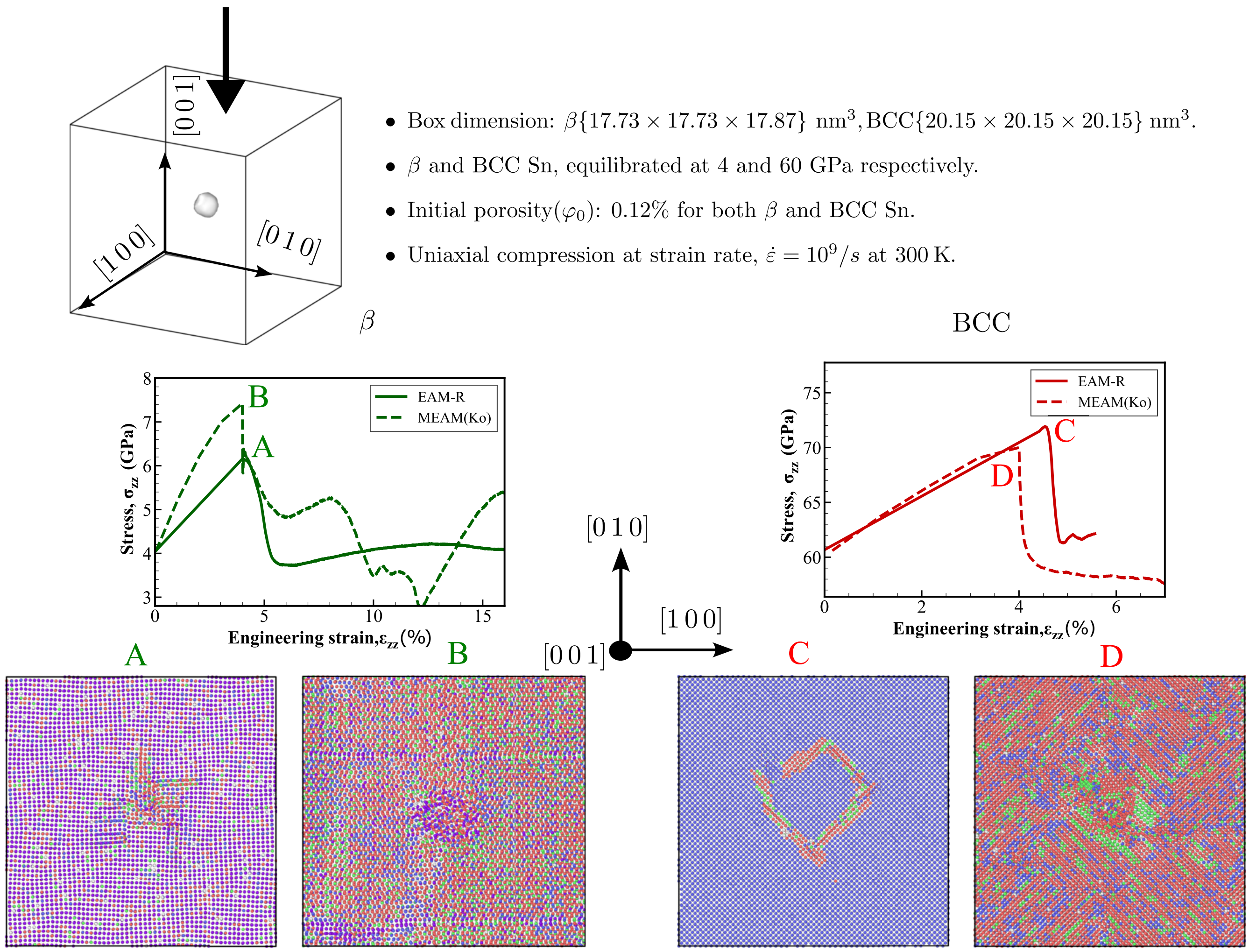

- Box dimension: $\beta\{17.73 \times 17.73 \times 17.87\}$ nm^3, BCC$\{20.15 \times 20.15 \times 20.15\}$ nm^3.
- β and BCC Sn, equilibrated at 4 and 60 GPa respectively.
- Initial porosity(φ_0): 0.12% for both β and BCC Sn.
- Uniaxial compression at strain rate, $\dot{\varepsilon} = 10^9/s$ at 300 K.

FIG. 11. β and BCC-Sn is subjected to uniaxial compression loading at strain rate, $\dot{\varepsilon} = 10^9/\mathrm{s}$.

to the EAM formalism. A neural-network-based approach, termed RANN, was used to train the ML potential using DFT calculations for Sn to predict the phase diagram of Sn as a function of pressure. While only energies were used in the training dataset, the hybrid EAM-R potential also accurately predicted the forces obtained from DFT. This potential was in excellent agreement with the experimental results pertaining to various properties of Sn but especially the high-pressure behavior. This potential demonstrates that it is necessary to add an underlying physics model to the ML potentials to create a stable interatomic potential. Currently, this potential represents the only interatomic potential that can quantitatively replicate phase transitions in Sn under high pressure. This method is generally applicable to other elements and multicomponent systems that require a high level of accuracy. While this potential is ~20 times slower than MEAM, it is fast enough to run MD on million-atom systems. Additionally, upon the creation of a database, this potential can now be rapidly fit within 5–10 mins. In general, this potential defines a paradigm for ML potentials and can be confidently used to obtain insights into deformation mechanisms of complex materials.

The DFT training database, calibration software, LAMMPS version with EAM-R package, and sample input script to run the potential are available in the RANN GitHub repository [103].

---

[1] W. Paul, Band structure of the intermetallic semiconductors from pressure experiments, J. Appl. Phys. **32**, 2082 (1961).

[2] T. G. Plymate, J. H. Stout, and M. E. Cavaleri, Pressure-volume-temperature behavior and heterogeneous equilibria of the non-quenchable body-centered tetragonal polymorph of metallic tin, J. Phys. Chem. Solids **49**, 1339 (1988).

[3] B. H. Cheong and K.-J. Chang, First-principles study of the structural properties of Sn under pressure, Phys. Rev. B **44**, 4103 (1991).

[4] J. Ihm and M. L. Cohen, Equilibrium properties and the phase transition of grey and white tin, Phys. Rev. B **23**, 1576 (1981).

[5] A. Roshanghias, J. Vrestal, A. Yakymovych, K. W. Richter, and H. Ipser, Sn–Ag–Cu nanosolders: Melting behavior and

phase diagram prediction in the Sn-rich corner of the ternary system, Calphad **49**, 101 (2015).

[6] B. Scrosati and J. Garche, Lithium batteries: Status, prospects and future, J. Power Sources **195**, 2419 (2010).

[7] J. Allain, D. Ruzic, and M. Hendricks, D, He and Li sputtering of liquid eutectic Sn–Li, J. Nucl. Mater. **290-293**, 33 (2001).

[8] J. Coenen, G. De Temmerman, G. Federici, V. Philipps, G. Sergienko, G. Strohmayer, A. Terra, B. Unterberg, T. Wegener, and D. Van den Bekerom, Liquid metals as alternative solution for the power exhaust of future fusion devices: Status and perspective, Phys. Scr. **2014**, 014037 (2014).

[9] J. Hafner, Atomic-scale computational materials science, Acta Mater. **48**, 71 (2000).

[10] E. van der Giessen, P. A. Schultz, N. Bertin, V. V. Bulatov, W. Cai, G. Csányi, S. M. Foiles, M. G. Geers, C. González, M. Hütter *et al.*, Roadmap on multiscale materials modeling, Modell. Simul. Mater. Sci. Eng. **28**, 043001 (2020).

[11] H. Olijnyk and W. Holzapfel, Phase transitions in Si, Ge and Sn under pressure, J. Phys. Colloques **45**, C8-153 (1984).

[12] M. Hanfland, U. Schwarz, K. Syassen, and K. Takemura, Crystal Structure of the High-Pressure Phase Silicon VI, Phys. Rev. Lett. **82**, 1197 (1999).

[13] M. I. McMahon, R. J. Nelmes, N. G. Wright, and D. R. Allan, Pressure dependence of the $Imma$ phase of silicon, Phys. Rev. B **50**, 739 (1994).

[14] M. Musgrave, On the relation between grey and white tin (α-Sn and β-Sn), Proc. R. Soc. Lond. A **272**, 503 (1963).

[15] J. D. Barnett, V. E. Bean, and H. T. Hall, X-ray diffraction studies on tin to 100 kilobars, J. Appl. Phys. **37**, 875 (1966).

[16] M. Liu and L.-G. Liu, Compressions and phase transitions of tin to half a megabar, High Temp. High Press. **18**, 79 (1986).

[17] Y. Yao and D. D. Klug, Prediction of a bcc–hcp phase transition for Sn: A first-principles study, Solid State Commun. **151**, 1873 (2011).

[18] A. Salamat, G. Garbarino, A. Dewaele, P. Bouvier, S. Petitgirard, C. J. Pickard, P. F. McMillan, and M. Mezouar, Dense close-packed phase of tin above 157 GPa observed experimentally via angle-dispersive x-ray diffraction, Phys. Rev. B **84**, 140104(R) (2011).

[19] M. S. Daw and M. I. Baskes, Embedded-atom method: Derivation and application to impurities, surfaces, and other defects in metals, Phys. Rev. B **29**, 6443 (1984).

[20] F. Sapozhnikov, G. Ionov, V. Dremov, L. Soulard, and O. Durand, The embedded atom model and large-scale md simulation of tin under shock loading, J. Phys. Conf. Ser. **500**, 032017 (2014).

[21] R. Ravelo and M. Baskes, Equilibrium and Thermodynamic Properties of Grey, White, and Liquid Tin, Phys. Rev. Lett. **79**, 2482 (1997).

[22] J. R. Vella, M. Chen, F. H. Stillinger, E. A. Carter, P. G. Debenedetti, and A. Z. Panagiotopoulos, Structural and dynamic properties of liquid tin from a new modified embedded-atom method force field, Phys. Rev. B **95**, 064202 (2017).

[23] S. A. Etesami, M. I. Baskes, M. Laradji, and E. Asadi, Thermodynamics of solid Sn and PbSn liquid mixtures using molecular dynamics simulations, Acta Mater. **161**, 320 (2018).

[24] M. I. Baskes, Modified embedded-atom potentials for cubic materials and impurities, Phys. Rev. B **46**, 2727 (1992).

[25] W.-S. Ko, D.-H. Kim, Y.-J. Kwon, and M. H. Lee, Atomistic simulations of pure tin based on a new modified embedded-atom method interatomic potential, Metals **8**, 900 (2018).

[26] B.-J. Lee, M. I. Baskes, H. Kim, and Y. K. Cho, Second nearest-neighbor modified embedded atom method potentials for bcc transition metals, Phys. Rev. B **64**, 184102 (2001).

[27] J. Behler, Perspective: Machine learning potentials for atomistic simulations, J. Chem. Phys. **145**, 170901 (2016).

[28] V. L. Deringer, M. A. Caro, and G. Csányi, Machine learning interatomic potentials as emerging tools for materials science, Adv. Mater. **31**, 1902765 (2019).

[29] Y. Zuo, C. Chen, X. Li, Z. Deng, Y. Chen, J. Behler, G. Csányi, A. V. Shapeev, A. P. Thompson, M. A. Wood *et al.*, Performance and cost assessment of machine learning interatomic potentials, J. Phys. Chem. A **124**, 731 (2020).

[30] T. Morawietz and N. Artrith, Machine learning-accelerated quantum mechanics-based atomistic simulations for industrial applications, J. Comput.-Aided Mol. Des. **35**, 557 (2021).

[31] J. S. Smith, B. Nebgen, N. Mathew, J. Chen, N. Lubbers, L. Burakovsky, S. Tretiak, H. A. Nam, T. Germann, S. Fensin *et al.*, Automated discovery of a robust interatomic potential for aluminum, Nat. Commun. **12**, 1 (2021).

[32] R. Batra, L. Song, and R. Ramprasad, Emerging materials intelligence ecosystems propelled by machine learning, Nat. Rev. Mater. **6**, 655 (2021).

[33] J. E. Saal, A. O. Oliynyk, and B. Meredig, Machine learning in materials discovery: Confirmed predictions and their underlying approaches, Annu. Rev. Mater. Res. **50**, 49 (2020).

[34] B. L. DeCost, J. R. Hattrick-Simpers, Z. Trautt, A. G. Kusne, E. Campo, and M. L. Green, Scientific AI in materials science: A path to a sustainable and scalable paradigm, Mach. Learn.: Sci. Technol. **1**, 033001 (2020).

[35] M. Picklum and M. Beetz, Matcalo: Knowledge-enabled machine learning in materials science, Comput. Mater. Sci. **163**, 50 (2019).

[36] J. J. de Pablo, N. E. Jackson, M. A. Webb, L.-Q. Chen, J. E. Moore, D. Morgan, R. Jacobs, T. Pollock, D. G. Schlom, E. S. Toberer *et al.*, New frontiers for the materials genome initiative, npj Comput. Mater. **5**, 41 (2019).

[37] S. P. Ong, Accelerating materials science with high-throughput computations and machine learning, Comput. Mater. Sci. **161**, 143 (2019).

[38] H. Mori and T. Ozaki, Neural network atomic potential to investigate the dislocation dynamics in bcc iron, Phys. Rev. Mater. **4**, 040601(R) (2020).

[39] N. Artrith and A. Urban, An implementation of artificial neural-network potentials for atomistic materials simulations: Performance for TiO_2, Comput. Mater. Sci. **114**, 135 (2016).

[40] Y.-S. Lin, G. P. P. Pun, and Y. Mishin, Development of a physically-informed neural network interatomic potential for tantalum, Comput. Mater. Sci. **205**, 111180 (2022).

[41] R. Z. Khaliullin, H. Eshet, T. D. Kühne, J. Behler, and M. Parrinello, Nucleation mechanism for the direct graphite-to-diamond phase transition, Nat. Mater. **10**, 693 (2011).

[42] G. C. Sosso, G. Miceli, S. Caravati, J. Behler, and M. Bernasconi, Neural network interatomic potential for the phase change material gete, Phys. Rev. B **85**, 174103 (2012).

[43] M. A. Cusentino, M. A. Wood, and A. P. Thompson, Explicit multielement extension of the spectral neighbor analysis po-

tential for chemically complex systems, J. Phys. Chem. A **124**, 5456 (2020).

[44] A. P. Thompson, L. P. Swiler, C. R. Trott, S. M. Foiles, and G. J. Tucker, Spectral neighbor analysis method for automated generation of quantum-accurate interatomic potentials, J. Comput. Phys. **285**, 316 (2015).

[45] D. Dickel, M. Nitol, and C. Barrett, Lammps implementation of rapid artificial neural network derived interatomic potentials, Comput. Mater. Sci. **196**, 110481 (2021).

[46] M. S. Nitol, D. E. Dickel, and C. D. Barrett, Artificial neural network potential for pure zinc, Comput. Mater. Sci. **188**, 110207 (2021).

[47] M. S. Nitol, D. E. Dickel, and C. D. Barrett, Machine learning models for predictive materials science from fundamental physics: An application to titanium and zirconium, Acta Mater. **224**, 117347 (2022).

[48] M. S. Nitol, S. Mun, D. E. Dickel, and C. D. Barrett, Unraveling Mg $\langle c + a \rangle$ slip using neural network potential, Philos. Mag. **102**, 651 (2022).

[49] P. Giannozzi, S. Baroni, N. Bonini, M. Calandra, R. Car, C. Cavazzoni, D. Ceresoli, G. L. Chiarotti, M. Cococcioni, I. Dabo *et al.*, QUANTUM ESPRESSO: a modular and open-source software project for quantum simulations of materials, J. Phys.: Condens. Matter **21**, 395502 (2009), https://github.com/QEF/q-e/releases/tag/qe-6.4.1.

[50] J. P. Perdew, K. Burke, and M. Ernzerhof, Generalized Gradient Approximation Made Simple, Phys. Rev. Lett. **77**, 3865 (1996).

[51] D. A. Rehn, C. W. Greeff, D. G. Sheppard, and S. D. Crockett, Using density functional theory to construct multiphase equations of state: Tin as an example, Los Alamos National Laboratory Tech. Rep. No. LA-UR-20-29170 (2020).

[52] R. Armiento and A. E. Mattsson, Functional designed to include surface effects in self-consistent density functional theory, Phys. Rev. B **72**, 085108 (2005).

[53] H. J. Monkhorst and J. D. Pack, Special points for Brillouin-zone integrations, Phys. Rev. B **13**, 5188 (1976).

[54] N. Marzari, D. Vanderbilt, A. De Vita, and M. C. Payne, Thermal Contraction and Disordering of the Al(110) Surface, Phys. Rev. Lett. **82**, 3296 (1999).

[55] M. I. Baskes, S. G. Srinivasan, S. M. Valone, and R. G. Hoagland, Multistate modified embedded atom method, Phys. Rev. B **75**, 094113 (2007).

[56] J. Behler and M. Parrinello, Generalized Neural-Network Representation of High-Dimensional Potential-Energy Surfaces, Phys. Rev. Lett. **98**, 146401 (2007).

[57] M. I. Baskes, Determination of modified embedded atom method parameters for nickel, Mater. Chem. Phys. **50**, 152 (1997).

[58] G. Pun, R. Batra, R. Ramprasad, and Y. Mishin, Physically informed artificial neural networks for atomistic modeling of materials, Nat. Commun. **10**, 2339 (2019).

[59] D. W. Marquardt, An algorithm for least-squares estimation of nonlinear parameters, J. Soc. Ind. Appl. Math. **11**, 431 (1963).

[60] K. Levenberg, A method for the solution of certain non-linear problems in least squares, Q. Appl. Math. **2**, 164 (1944).

[61] T. Chen, F. Yuan, J. Liu, H. Geng, L. Zhang, H. Wang, and M. Chen, Modeling the high-pressure solid and liquid phases of tin from deep potentials with *ab initio* accuracy, arXiv:2209.05059.

[62] C. S. Barrett and T. B. Massalski, *Structure of Metals: Crystallographic Methods, Principles, and Data*, 3rd ed., edited by C. S. Barrett and T. B. Massalski (Pergamon Press, Oxford, 1980).

[63] C. Kittel, *Introduction to Solid State Physics*, 8th ed. (John Wiley & Sons, Inc., Hoboken, 2005).

[64] W. F. Gale and T. C. Totemeier, *Smithells Metals Reference Book*, 8th ed., edited by W. F. Gale and T. C. Totemeir (Elsevier, Oxford, 2004).

[65] A. Salamat, R. Briggs, P. Bouvier, S. Petitgirard, A. Dewaele, M. E. Cutler, F. Cora, D. Daisenberger, G. Garbarino, and P. F. McMillan, High-pressure structural transformations of Sn up to 138 GPa: Angle-dispersive synchrotron x-ray diffraction study, Phys. Rev. B **88**, 104104 (2013).

[66] J. Byggmästar, K. Nordlund, and F. Djurabekova, Gaussian approximation potentials for body-centered-cubic transition metals, Phys. Rev. Mater. **4**, 093802 (2020).

[67] X.-G. Li, C. Chen, H. Zheng, and S. P. Ong, Complex strengthening mechanisms in the NbMoTaW multi-principal element alloy, arXiv:1912.01789.

[68] A. Van der Ven and G. Ceder, The thermodynamics of decohesion, Acta Mater. **52**, 1223 (2004).

[69] F. Yang and J. Li, Deformation behavior of tin and some tin alloys, J. Mater. Sci. Mater. Electron **18**, 191 (2007).

[70] V. Vítek, Intrinsic stacking faults in body-centred cubic crystals, Philos. Mag. **18**, 773 (1968).

[71] J. A. Zimmerman, H. Gao, and F. F. Abraham, Generalized stacking fault energies for embedded atom fcc metals, Modell. Simul. Mater. Sci. Eng. **8**, 103 (2000).

[72] A. Telang and T. Bieler, The orientation imaging microscopy of lead-free Sn-Ag solder joints, JOM **57**, 44 (2005).

[73] M. Bhatia, I. Adlakha, G. Lu, and K. Solanki, Generalized stacking fault energies and slip in β-tin, Scr. Mater. **123**, 21 (2016).

[74] G. Deffrennes, P. Faure, F. Bottin, J.-M. Joubert, and B. Oudot, Tin (Sn) at high pressure: Review, X-ray diffraction, DFT calculations, and Gibbs energy modeling, J. Alloys Compd. **919**, 165675 (2022).

[75] S. Plimpton, Fast parallel algorithms for short-range molecular dynamics, J. Comput. Phys. **117**, 1 (1995).

[76] E. A. Brandes and G. B. Brook, *Smithells Metals Reference Book*, 7th ed., edited by E. A. Brandes and G. B. Brook (Butterworth-Heinemann, Oxford, 1992).

[77] P. G. Harrison, in *Chemistry of Tin*, 1st ed., edited by P. J. Smith (Springer, Dordrecht, 1989).

[78] I. Barin, O. Knacke, and O. Kubaschewski, *Thermochemical Properties of Inorganic Substances: Supplement* (Springer-Verlag, Berlin, Heidelberg, 1977).

[79] P. M. Larsen, S. Schmidt, and J. Schiøtz, Robust structural identification via polyhedral template matching, Modell. Simul. Mater. Sci. Eng. **24**, 055007 (2016).

[80] A. Stukowski, Visualization and analysis of atomistic simulation data with OVITO—The Open Visualization Tool, Modell. Simul. Mater. Sci. Eng. **18**, 015012 (2010).

[81] D. E. Dickel and C. D. Barrett, Methods for the determination of diffusionless transformation conditions from atomistic simulations, Modell. Simul. Mater. Sci. Eng. **27**, 023001 (2019).

[82] F. Vnuk, A. De Monte, and R. Smith, The effect of pressure on the semiconductor-to-metal transition temperature in tin and in dilute Sn–Ge alloys, J. Appl. Phys. **55**, 4171 (1984).

[83] C. Yu, J. Liu, H. Lu, and J. Chen, *Ab initio* calculation of the properties and pressure induced transition of Sn, Solid State Commun. **140**, 538 (2006).

[84] A. Aguado, First-principles study of elastic properties and pressure-induced phase transitions of Sn: LDA versus GGA results, Phys. Rev. B **67**, 212104 (2003).

[85] R. Jeffery, J. D. Barnett, H. Vanfleet, and H. T. Hall, Pressure calibration to 100 kbar based on the compression of NaCl, J. Appl. Phys. **37**, 3172 (1966).

[86] A. Ohtani, S. Mizukami, M. Katayama, A. Onodera, and N. Kawai, Multi-anvil apparatus for high pressure x-ray diffraction, Jpn. J. Appl. Phys. **16**, 1843 (1977).

[87] R. Briggs, D. Daisenberger, O. T. Lord, A. Salamat, E. Bailey, M. J. Walter, and P. F. McMillan, High-pressure melting behavior of tin up to 105 GPa, Phys. Rev. B **95**, 054102 (2017).

[88] B. Schwager, M. Ross, S. Japel, and R. Boehler, Melting of Sn at high pressure: Comparisons with Pb, J. Chem. Phys. **133**, 084501 (2010).

[89] R. Briggs, D. Daisenberger, A. Salamat, G. Garbarino, M. Mezouar, M. Wilson, and P. McMillan, Melting of Sn to 1 Mbar, J. Phys.: Conf. Ser. **377**, 012035 (2012).

[90] S. Desgreniers, Y. K. Vohra, and A. L. Ruoff, Tin at high pressure: An energy-dispersive x-ray-diffraction study to 120 GPa, Phys. Rev. B **39**, 10359 (1989).

[91] S. Weir, M. Lipp, S. Falabella, G. Samudrala, and Y. Vohra, High pressure melting curve of tin measured using an internal resistive heating technique to 45 GPa, J. Appl. Phys. **111**, 123529 (2012).

[92] H. Gamsjäger, T. Gadja, J. Sangster, S. Saxena, and W. Voigt, *Chemical Thermodynamics—Chemical Thermodynamics of Tin*, edited by J. Perrone (OECD, Issy-les-Moulineaux, 2012), Vol. 12.

[93] H. Preston-Thomas, The International Temperature Scale of 1990 (ITS-90), Metrologia **27**, 3 (1990).

[94] J. D. Barnett, R. B. Bennion, and H. T. Hall, X-ray diffraction studies on tin at high pressure and high temperature, Science **141**, 1041 (1963).

[95] A. I. Kingon and J. B. Clark, A redetermination of the melting curve of tin to 3.7 GPa, High Temp. High Press. **12**, 75 (1980).

[96] M. L. McDaniel, S. E. Babb Jr, and G. J. Scott, Melting curves of five metals under high pressure, J. Chem. Phys. **37**, 822 (1962).

[97] L. Xu, Y. Bi, X. Li, Y. Wang, X. Cao, L. Cai, Z. Wang, and C. Meng, Phase diagram of tin determined by sound velocity measurements on multi-anvil apparatus up to 5 GPa and 800 K, J. Appl. Phys. **115**, 164903 (2014).

[98] N. Rambert, B. Sitaud, and P. Faure, Equation d'état multiphase et courbe de fusion de l'étain sous pression: une nouvelle approche expérimentale, Rapport CEA A-22F00-00-10 (2003).

[99] H. Mii, I. Fujishiro, and T. Nomura, Les propriétés physiques des solides sous pression, Colloq. C. N. R. S 441 (1968).

[100] G. C. Kennedy and R. Newton, Solid–liquid and solid–solid phase transitions in some pure metals at high temperatures and pressures, Solids Under Pressure 163 (1963).

[101] R. Stager, A. Balchan, and H. Drickamer, High-pressure phase transition in metallic tin, J. Chem. Phys. **37**, 1154 (1962).

[102] B. Kiefer, T. Duffy, T. Uchida, and Y. Wang, Melting of tin at high pressures, APS User Activity Report (2002).

[103] https://github.com/MashoorNitol/Hybrid-RANN-EAM.